Journal of Materials Research and Technology 40 (2026) 2569–2583

Contents lists available at ScienceDirect

Journal of Materials Research and Technology

journal homepage: www.elsevier.com/locate/jmrt

Fatigue softening mechanisms in UFG-EUROFER97 steel. A microstructural study

Marcello Cabibbo [a,*], Dario Croccolo [b], Andrea Di Schino [c], Roberto Montanari [d,**], Giorgio Olmi [b], Giulia Stornelli [c], Claudio Testani [e], Alessandra Varone [d]

[a] Department of Industrial Engineering and Mathematical Sciences (DIISM), Università Politecnica delle Marche, 60131 Ancona, Italy
[b] Department of Industrial Engineering (DIN), University of Bologna, 40126 Bologna, Italy
[c] Department of Engineering, University of Perugia, 06125 Perugia, Italy
[d] Department of Industrial Engineering, University of Rome Tor Vergata, 00133 Rome, Italy
[e] CALEF-ENEA CR-Casaccia, S. Maria di Galeria, 00123 Rome, Italy

ARTICLE INFO

Keywords:
EUROFER97 steel
Nuclear applications
Thermo-mechanical treatment
Fatigue
Microstructure
Softening

ABSTRACT

A novel Thermo-Mechanical Treatment (TMT) developed by us leads to a microstructure with Ultra-Fine Grains (UFG) resulting in improved mechanical properties compared to those of standard EUROFER97 steel, foreseen for nuclear fusion applications. Since softening was observed after High Cycle Fatigue (HCF) tests at room temperature, this work investigated the specific microstructural mechanisms. The microstructure evolution of fatigued samples has been studied by means of Electron Back-Scattered Diffraction (EBSD), X-Ray Diffraction (XRD), Transmission Electron Microscopy (TEM) and Scanning Electron Microscopy (SEM). Softening resulted to be originated by the phenomenon of fatigue-assisted grain coarsening. HCF always leads to the increase of grain and sub-grain size together with texture change, and such modifications depend on the stress level. Under cyclic stress, boundary migration and absorption in the boundaries of dislocations produced by Frank-Read sources inside the grains lead to an excess of dislocations in the boundaries. Although the stability and mobility of High-Angle Grain Boundaries (HAGBs) and Low-Angle Grain Boundaries (LAGBs) are totally different, both the boundaries become unstable. In the final step of the process, the collapse or sliding of unstable HAGBs and LAGBs give rise to a population of grains and sub-grains of larger size. The novel TMT demonstrates improved softening behavior compared to standard EUROFER97, and the results obtained will guide future research toward further improvements.

1. Introduction

The increase of irradiation resistance is one of the most challenging problems in the development of structural materials for DEMO reactor and future commercial fusion power plants [1–4]. Atomic displacements caused by energetic neutrons lead to the formation of many lattice defects, resulting in material embrittlement [5–7]. Another contribution to brittleness comes from He and H produced by nuclear transmutation [8,9]. Reduced-Activation Ferritic-Martensitic (RAFM) steels are candidates for the structural parts of future nuclear fusion plants and fission reactors of IV generation [10], and among them, EUROFER97 is the European reference steel [11–14]. EUROFER97 steel plates (14 mm thick) are usually produced by hot rolling followed by austenitization treatment (980 °C for 30 min), air quenching and tempering (760 °C for 90 min) [15]. The result of this treatment, hereinafter referred as 'standard', is a microstructure consisting of tempered martensite.

Based on currently available neutron irradiation data some doubts have been raised about the use of EUROFER97 for the DEMO reactor in 'the water-cooled blanket' configuration [16–18]. In fact, it exhibits good irradiation resistance above 350 °C, but the water-cooled blanket is foreseen to operate in the temperature range of 280–350 °C [19] and irradiation at temperature below 350 °C leads to excessive brittleness and increases the Ductile-Brittle Transition Temperature (DBTT) [4].

Grain refinement is one of the most promising strategies to improve both He susceptibility in RAFM steels [20,21] and reduce DBTT [21]. Grain refinement reduces the DBTT because of the larger number of

* Corresponding author.
** Corresponding author.
E-mail addresses: m.cabibbo@staff.univpm.it (M. Cabibbo), roberto.montanari@uniroma2.it (R. Montanari).

https://doi.org/10.1016/j.jmrt.2026.01.009
Received 11 November 2025; Received in revised form 29 December 2025; Accepted 2 January 2026
Available online 2 January 2026

grain boundaries which act as barriers for the propagation of cleavage cracks. Grain boundaries also represent preferred sites for He bubble nucleation. According to the theoretical model of Mansur and Coghlan [22], below a critical number of He atoms inside the bubbles, they are stable whereas above such critical value they expand giving rise to swelling and embrittlement of the steel. Therefore, grain refinement guarantees the presence of many bubble nucleation sites which lead to a more favorable partition of He atoms and retard the bubble growth.

Various approaches have been considered to reduce the average grain size of EUROFER97 steel [23], including double austenitization treatment [24], Equal Channel Angular Pressing (ECAP) [25] and High-Pressure Torsion (HPT) [26]. A novel Thermo-Mechanical Treatment (TMT) developed by some of the present investigators [27–30] yields Ultra-Fine Grains (UFG) which strengthen the material without detrimental effects on its ductility. An extended experimental campaign combining different cold rolling reduction ratios (CR) and treatment temperatures showed that the best condition corresponds to a CR of 80 % and treatment at 650 °C for 1 h. It allows to obtain a fully recrystallized material avoiding the onset of grain growth; in this way the ultra-fine size of grains guarantees improved mechanical properties compared to those of standard EUROFER97. The data reported in Table 1 highlight the effectiveness of this TMT.

The operation pulsed mode of fusion reactors will expose structural materials to complex thermo-mechanical loads and consequently causes fatigue damage [32,33]. Therefore, the High Cycle Fatigue (HCF) behavior of UFG EUROFER97 was also investigated, and fatigue strength resulted to be comparable to that of standard EUROFER97 [34]. Moreover, due to fatigue cycles, softening was observed with hardness reduction proportional to the applied load.

According to current research studies on fatigue which take a mechanism-based approach rather than a purely empirical one [35,36], this work was carried out to better understand the mechanisms behind softening. To this scope, Electron Back-Scattered Diffraction (EBSD) measurements, X-Ray Diffraction (XRD) analyses, Transmission Electron Microscopy (TEM) observations and Scanning Electron Microscopy (SEM) investigations of fracture surfaces were carried out on some selected samples of UFG EUROFER97 steel subjected to HCF.

2. Material and methods

The measured chemical composition of EUROFER97 steel (batch 2) is very close to the nominal one and is reported in Table 2.

A plate of standard EUROFER97 was cold rolled with an 80 % reduction ratio, and then flat samples (see Fig. 1) for fatigue tests were cut using Electrical Discharge Machining (EDM). Each sample was heat treated at 650 °C for 1 h in an argon atmosphere and examined by light microscopy (LM-Union Optical Co., Ltd., Tokyo, Japan) to exclude the presence of significant defects. The dimensions of all the samples were measured to properly correlate the applied load to the resulting stress during fatigue tests. This procedure was done because EDM cutting may introduce slight deviations from the nominal dimensions. The standard deviations were lower than 0.036 mm. Finally, roughness (RT-25, Alpa Metrology, Brescia, Italy) was measured at the gauge on both sides of each sample (six measurements); the average Ra = 0.027 ± 0.006 μm is consistent with recommendations of many standards of fatigue testing [37].

HCF tests were performed by using a resonant machine (20 kN capacity, by Rumul Switzerland) under tension - tension with a stress ratio R = 0.2 and at the frequency f = 113 Hz. The trial was carried out under load control, and the breakage was considered at the moment of crack initiation and the run-out was set at 10^7 cycles. More details about fatigue tests can be found in Ref. [34].

Table 1
Yield Stress (YS), Ultimate Tensile Stress (UTS), uniform elongation (Au%), and total elongation (A%) of UFG EUROFER97 in comparison to Standard EUROFER97 [31].

Steel	YS (MPa)	UTS (MPa)	Au (%)	A (%)
UFG EUROFER97 [30]	644	714	13.4	23.1
Standard EUROFER97 [31]	547	683	6.5	21.6

Table 2
Chemical composition of EUROFER97 expressed in wt.% (Fe to balance).

Cr	C	Mn	V	W	Ta	Ti	N
8.91	0.12	0.48	0.2	1.09	0.14	0.009	0.019
P	**S**	**B**	**Si**	**Nb**	**Mo**	**Ni**	**Cu**
<0.005	0.004	<0.001	0.006	0.0018	0.0015	0.002	0.003

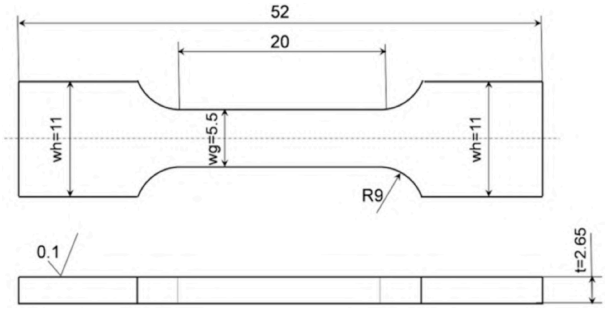

Fig. 1. Drawing of the samples used in fatigue tests. Dimensions are expressed in mm.

Four samples were chosen for TEM, EBSD and XRD analyses: (1) not subjected to fatigue test, (2) not broken in fatigue tests, (3) broken after a great number of cycles, (4) broken after a lower number of cycles. The results of the fatigue tests are reported in Table 3, along with Vickers hardness HV_5 values measured on the surface of the samples, which show softening in all of them. The maximum hardness reduction, observed in sample 4, is approximately 5 % [34].

The microstructure of all the samples was examined by XRD, EBSD and TEM.

XRD measurements were carried out to determine texture, dislocation density ρ and average size of coherently diffracting domains $< D >$. XRD patterns were recorded in the 2 θ range 15°–55° using the Mo-Kα radiation (λ = 0.070926 nm) with 2 θ steps of 0.05° and a counting time per step of 2 s. In broken fatigue samples (3 and 4) the X-ray beam was focused near the fracture border.

Preferred grain orientation was evaluated by comparing the relative peak intensities of the strongest reflections to those reported in the JCPDS database (file 6–696) for Fe with randomly oriented grains [38]. The texture was described by the parameter χ, namely the ratio between the relative intensities of XRD peaks determined through experiments $(I/I_0)_{EXP}$ and the reference ones in the database, $(I/I_0)_{REF}$:

$$\chi = \left(\frac{I}{I_0}\right)_{EXP} \Big/ \left(\frac{I}{I_0}\right)_{REF} \quad (1)$$

Dislocation density and size of crystalline domains were determined from the full width at half maximum (β_T) of precision peak profiles recorded with 2 θ steps of 0.005° and a counting time per step of 4 s. The experimental profiles were corrected from the Kα2 component by fitting with Lorentzian curves and the full width at half maximum of the Kα1 component β_T was obtained by subtracting the instrumental broadening. β_T is the sum of two contributions, β_D and β_ε, due to $< D >$ and microstrains ε, respectively:

$$\beta_T = \beta_D + \beta_\varepsilon = \frac{0.89\,\lambda}{< D > \cos\theta} + 2\,\varepsilon\,\tan\theta \quad (2)$$

Once obtained $< D >$ and ε by means of the Cauchy procedure, the dislocation density was calculated through the Williamson-Smallman

Table 3
Results of fatigue tests and hardness of UFG EUROFER97 [34].

ID	Sample	σmax (MPa)	σmin (MPa)	Δσ (MPa)	εmax (%)	εmin (%)	Outcome	Observed life	HV_5
1	Not tested	–	–	–			–	–	213
2	Tested	380	76	304	0.185	0.037	10.000.000	Run-out	209
3	Tested	440	88	352	0.214	0.043	176.200	Failure	205
4	Tested	500	100	400	0.244	0.049	48.800	Failure	204

equation [39]:

$$\rho = \frac{\Phi\, \varepsilon^2}{F b^2} \tag{3}$$

being $\Phi = 16.1$ a constant, $F \approx 1$ a factor depending on the interaction of dislocations and $b = 0.248$ nm the modulus of Burgers vector.

To determine the texture, average grain size, grain size distribution and typology of Grain Boundaries (GBs), EBSD measurements were performed using a Field Emission Gun Scanning Electron Microscope (FEG-SEM) (Ultra-Plus Carl-Zeiss-Oberkochen, Germany) equipped with an EBSD detector (C Nano Oxford Instruments, UK) with a step size of 0.05 μm.

Thin foils for TEM observations were extracted from the closest possible proximity section to the failed zones, whenever present, or from the highly stressed zone of the samples. Thin foils were then prepared by mechanical thinning and polishing down to a thickness of 70–80 μm, followed by dual-surface dimpling down to a thickness of 20–25 μm and finally ion-milled to electron transparency using a Gatan© (Gatan Inc., Pleasanton, CA, USA) PIPS working at 8 keV (incident beam angle progressively reducing to 8, 6, and 4°). TEM analyses were carried out by a Philips™ (Philips, Waltham, MA, USA) CM-200 microscope working at 200 kV and equipped with a double-tilt LN cooled specimen holder. Selected area diffraction patterns (SAEDP) were recorded by converged beam. All TEM inspections were carried out by tilting the thin discs to orient the crystal at [100] zone axis and selecting the g-vector at g = (002) diffraction condition to better highlight the tangled dislocations and the dislocations constituting the low-angle boundaries.

The fracture surfaces of samples 3 and 4, broken in HCF tests, were examined by FEG-SEM.

3. Results

The samples were prepared through a TMT that induces complete recrystallization, and the resulting microstructure consists of ultra-fine grains with an average size of 600 ± 60 nm and equiaxed shape [30]. The Bright Field (BF) TEM micrograph in Fig. 2 (a) shows the typical grain structure of the material. At higher magnification, a homogeneous distribution of carbides with mean size ranging from 4 to 10 nm spaced at distance of ~15 nm can be observed (Fig. 2 (b)).

Generally, GBs exhibit a regular shape with few local exceptions like that shown in Fig. 3 (a). As better evidenced in the detail of Fig. 3 (b), a part of the boundary is waved and associated with an area of higher dislocation density. Such irregularity involves a distinct mobility advantage over neighboring GBs.

The samples after HCF tests were examined by EBSD, XRD and TEM for monitoring their microstructural evolution.

Fig. 4 shows the EBSD maps and the Inverse Pole Figures (IPFs) of the original material (sample 1) and samples 2, 3 and 4 subjected to HCF. The data determined through these experiments are reported in Table 4. All the samples exhibit equiaxed grains and the average grain size $< d >$ progressively increases with the applied stress. The maps evidence the presence of extended zones of near-by oriented grains in all the samples. Another effect of HCF is the weakening of the strong [100] texture of the original material.

From the analysis of maps in Fig. 4 the distributions of grain sizes and misorientation angles between the grains were determined, and the results are shown in Figs. 5 and 6, respectively.

The grain size distributions follow a typical log-normal trend and the average values $< d >$, reported in Table 4, increase with applied stress. The narrow profiles of size distributions indicate that the grain growth induced by fatigue tests is homogeneous and only a few grains reach a

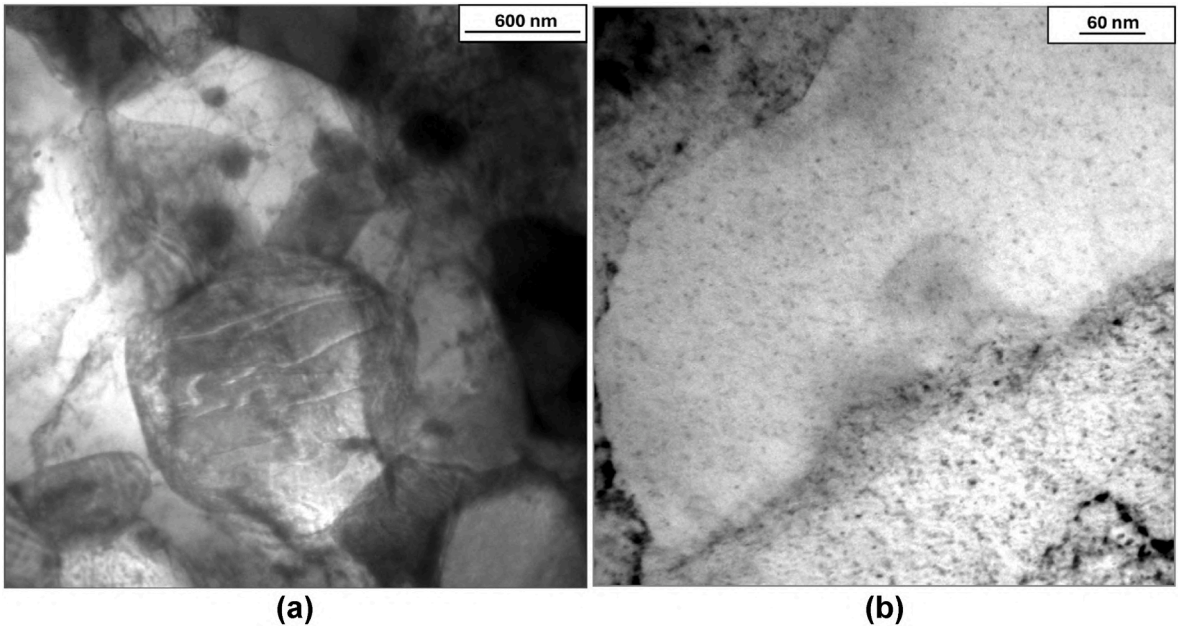

Fig. 2. Low-magnification BF-TEM micrograph showing the grain structure of the original material, not subjected to fatigue tests (a). At higher magnification, a homogeneous distribution of nanometric carbides is observed (b).

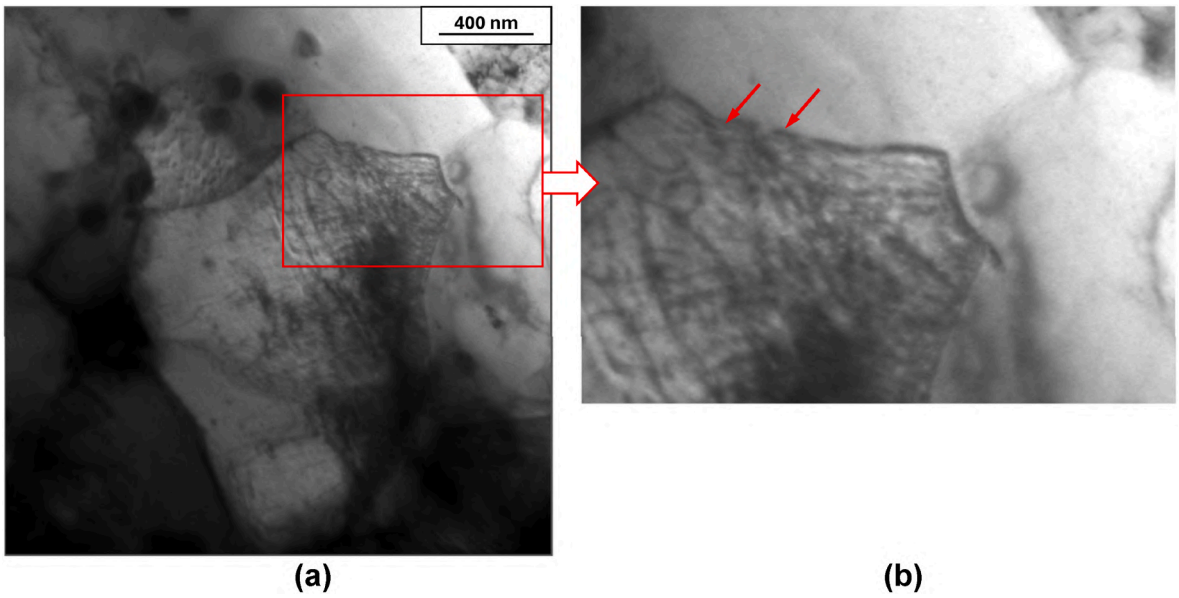

Fig. 3. Local irregularities of grain boundaries are observed near areas of dislocation accumulation (a). This feature is displayed at higher magnification in (b).

size above 2 μm.

The distributions of grain boundary misorientations evidence that both High-Angle Grain Boundaries (HAGBs, $\theta > 10°$) and Low-Angle Grain Boundaries (LAGBs, $2° < \theta \leq 10°$) are present in all the samples. After fatigue tests, the fractions of LAGBs and HAGBs change, indicating that instability in both of them is induced by the applied cyclic stress.

To reveal the possible presence of local dislocation structures due to crystal curvature, Kernel Average Misorientation (KAM) maps were also collected. They are displayed in Fig. 7 along with the corresponding distributions of misorientation angles. The average KAM angles determined by the analysis of these distributions are reported in Table 4.

As expected, relevant stress concentration sites are not present in the original material, thus the dislocations are homogeneously distributed. Significant variations are not observed after fatigue tests. The average KAM angle is 0.32° in EUROFER97 produced through the novel TMT and it slightly increases in the samples subjected to fatigue tests without relevant changes: its value does not exceed 0.46° (sample 3).

By considering the main Fe slip system, {110} <111>, the Schmid factor ζ of each sample was also determined from EBSD analysis (Table 4). It is a geometric value used to predict the activation of an individual slip mode with respect to a defined direction in a crystalline material during plastic deformation: the closer to 0.5 the value of the slip system, the easier its activation. Within the experimental error, this value turned out to be substantially the same for all the examined samples and very close to 0.5.

Fig. 8 (a) displays the XRD patterns of the examined samples, and the relative intensities of the strongest reflections, reported in Table 4, confirm EBSD results.

The comparison between the data of original material (sample 1) and those taken from the JCPDS database (file 6–696) [38] shows that the steel exhibits a strong [100] cubic texture with a secondary [211] component. After fatigue tests both components result weakened because χ_{200} and χ_{211} parameters decrease, indicating a change of grain orientations.

Fig. 8 (b) shows the precision {110} peak profiles of the samples examined. No mono-chromator was used in present XRD experiments thus each peak is the overlapping of the Kα1 and Kα2 reflection components. It is apparent that peak broadening reduces after fatigue tests and narrowing becomes more pronounced with increasing applied stress.

Dislocation density ρ and mean size $< D >$ of coherently diffracting domains have been determined to understand how they affect the peak narrowing observed in fatigued samples. For each sample, the value of $< D >$ is always smaller than the grain size $< d >$ measured through EBSD because XRD gives the average size of crystalline domains with reciprocal misorientation $< 1°$ whereas the angular resolution of EBSD does not allow to distinguish crystals with misorientation $< 2°$. In the present case, $< D >$ represents the size of sub-grains. The results reported in Table 4 reveal that the sizes of both grains and sub-grains progressively increase with the stress applied in fatigue tests together with the dislocation density ρ.

BF TEM micrographs in Fig. 9, taken at low magnification, show the grain structure of samples subjected to fatigue tests in different conditions and outcomes. From the comparison with the original material (Fig. 2 (a)) an increase of grain size is observed after HCF tests.

Micrographs at higher magnification (Fig. 10 (a) and (b) and (c)) evidence that fatigue induces a certain degree of LAGBs and HAGBs destructuration into tangled edge dislocations leading to either partial or complete collapse of boundaries and sub-boundaries. This phenomenon was observed in all the samples subjected to HCF.

The microstructure of fatigued samples is complex and exhibits different features; an example is given in Fig. 11 (sample 4). In Fig. 11 (a), a couple of collapsing GBs are observed. GBs consist of networks of edge and screw dislocations with a structure suitable to accommodate the misorientation between the two crystals. The micrograph shows the remnant of such a structure and the free dislocations produced in the process of boundary disaggregation near these boundaries. As indicated by the red arrow, the same image displays a pile-up of dislocations at a triple joint. Fig. 11 (b) shows a group of dislocations in an unstable GB. In Fig. 11 (c), a set of dislocations re-emitted by a GB is clearly detected. The dislocations are bowed thus they are subjected to stress. Such residual stress can be determined from their curvature radius R because it is yielded by $\tau = Gb/R$. The dislocations are fitted by a circle of $R = 280$ nm, the shear modulus $G = 81$ GPa thus τ results to be 72 MPa, a value compatible with the stress range σ_{min}-σ_{max} used to test the sample 4. Since the Burgers vector and the character of dislocations are unknown, this is a rough estimation representing only an upper bound for the residual stress. Moreover, inside several grains, there are dislocation dipoles like those shown in Fig. 11 (d).

Some waved boundaries are observed in all the fatigued samples and their frequency increases with the applied stress. An example is provided

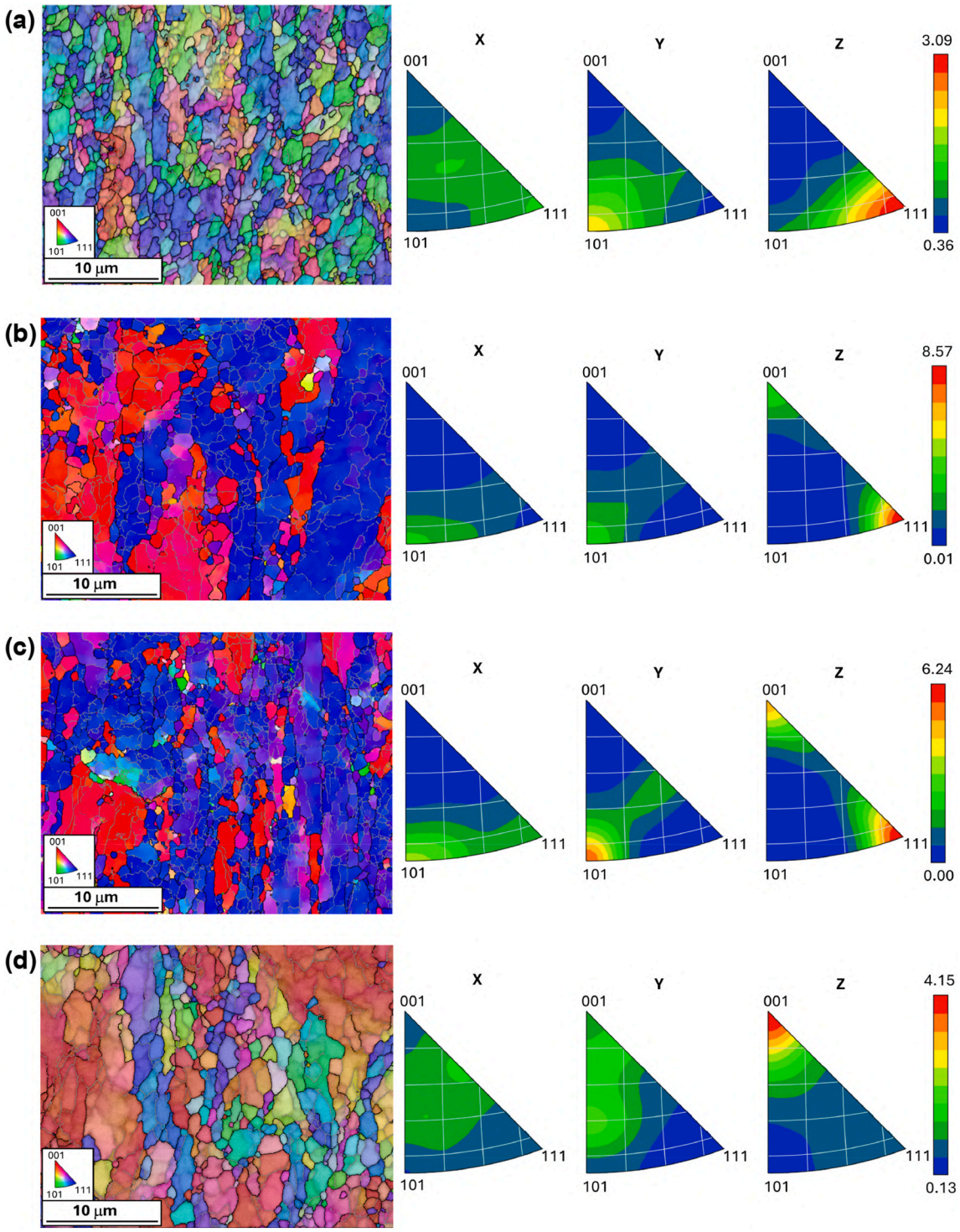

Fig. 4. EBSD maps and inverse pole figures of samples 1 (a), 2 (b), 3 (c) and 4 (d).

in Fig. 12, which shows the microstructure of sample 2. Anyway, the structure of grain boundaries remains substantially regular, as previously observed in the original material.

The fracture surfaces of samples 3 and 4, broken in HCF tests, were examined by means of SEM observations. There are no relevant differences between these samples, and the typical features are displayed in Fig. 13 (sample 4). The stage I (crack initiation) was not sufficiently defined for a deep characterization, however SEM inspections revealed that preferred crack nucleation sites correspond to surface imperfections due to the sample fabrication process.

At lower magnification (Fig. 13 (a)), tear ridges, representing discontinuities along the crack advancement path, can be observed on the surface. At higher magnification (Fig. 13 (b)), the steel exhibits the typical striation marks (spacing of ~10 μm) produced by HCF in a ductile material. In correspondence with striations there are cracks perpendicular to the fracture surface. The micrograph in Fig. 13 (c) shows slip bands inclined at ~ 45° with respect to the sample surface. As displayed by the detail in Fig. 13 (d) their thickness is ~1 μm, namely a value very close to the average grain size $< d >$ (873 ± 53 nm). The fracture surface also shows the presence of some voids of micrometric

Table 4
EBSD and XRD analysis of the original material (sample 1) and fatigued samples 2, 3 and 4. XRD: relative intensities I/I_0 of the strongest reflections, parameter χ of {200} and {211} reflections, average size of sub-grains $< D >$, and dislocation density ρ. Relative intensities from the JCPDS database file 6–696 [38] are reported for comparison. EBSD: average size of grains $< d >$, average KAM angles, average Schmid factor ζ, and fractions of LAGBs and HAGBs.

			Samples				
XRD		**{*hkl*}**	**JCPDS (6–696)**	**1**	**2**	**3**	**4**
	I/I_0	**110**	100	100	100	100	100
		200	20	66	22	35	52
		211	30	55	21	33	38
		220	10	6	24	7	10
		310	12	9	17	10	12
		222	6	4	9	13	4
	χ_{200}			3.30	1.10	1.17	2.60
	χ_{211}			1.83	0.70	1.10	1.27
	$< D >$ (nm)			210	325	408	445
	ρ (m^{-2})			1.0×10^{13}	5.0×10^{13}	8.0×10^{13}	1.1×10^{14}
EBSD	$< d >$ (nm)			600 ± 60	674 ± 78	704 ± 71	873 ± 53
	KAM (deg.)			0.32	0.44	0.46	0.37
	Schmid factor			0.45 ± 0.04	0.47 ± 0.02	0.47 ± 0.02	0.47 ± 0.04
	LAGBs (%)			45	50	52	36
	HAGBs (%)			55	50	48	64

size.

4. Discussion

EUROFER97 steel prepared through the innovative process has been tested at room temperature, i.e. at the homologous temperature $T/T_M = 0.17$ (solidus temperature $T_M = 1447$ °C [40]). The results show that cyclic loading always affects the microstructure of the material, with effects depending on the applied stress. As shown by the EBSD and XRD results reported in Table 4, HCF tests lead to the coarsening of grains and sub-grains involving a weakening of the original [100] texture. This process is accompanied by a moderate increase in dislocation density. Moreover, in comparison to the original material (sample 1), all the fatigued samples exhibit variations in the fractions of LAGBs and HAGBs.

4.1. Softening due to grain coarsening

Grain and sub-grain coarsening and dislocation density increase involve opposite effects on mechanical properties. However, the resulting softening indicates that the effect of coarsening is prevalent. These effects can be estimated by considering the strengthening mechanisms affecting the mechanical properties, namely: (i) solid solution (σ_{SS}), (ii) Bailey-Hirsch (σ_{BH}) due to dislocations, (iii) Hall-Petch (σ_{HP}) related to the size of grains or sub-grains and (iv) Orowan (σ_K) connected to the precipitates. The values of σ_{SS} and σ_K were calculated in a previous work [30] and resulted to be 85 and 113 MPa, respectively. In fact, these contributions can be considered constant because fatigue tests at room temperature do not affect the amounts of Cr and W in solid solution, and the size and distribution of carbides.

The Bailey-Hirsch stress σ_{BH} can be written as:

$$\sigma_{BH} = M\alpha Gb\rho^{1/2} \quad (4)$$

where $M = 2.9$ is the Taylor factor for b.c.c. metals and the parameter $\alpha = 0.24$ [41].

The Hall-Petch strengthening is obtained by the relationship:

$$\sigma_{HP} = \sigma_0 + K < D >^{-\frac{1}{2}} \quad (5)$$

being $\sigma_0 = 13$ MPa [42] the friction stress, i.e., the matrix yield stress for a grain of theoretically infinite size, $K = 0.18$ MPa $m^{1/2}$ and $< D >$ the average crystallite size. The strengthening contributions σ_{BH} and σ_{HP} for each sample have been calculated by substituting into Eqs. (4) and (5) the values of $< D >$ and ρ reported in Table 4. The results in Fig. 14 demonstrate that the major contribution to strengthening always comes from the sub-micrometric size of grains and the yield stress is mainly controlled by the contribution σ_{HP}.

With increased applied stress the Bailey-Hirsch stress σ_{BH} due to dislocations increases whereas σ_{HP} decreases, however it always remains the most relevant strengthening contribution. Therefore, the total strengthening σ_T, that is the sum of the four contributions, decreases with consequent softening of the material.

Of course, it was not possible to perform tensile tests on the samples subjected to fatigue tests and compare the calculated data to the experimental ones, however this has been done for sample 1: the yield stress YS = 644 MPa, reported in Tables 1 and is very close to the calculated value $\sigma_T = 653$ MPa. Moreover, for all the samples the ratio between the calculated values of σ_T, displayed in Fig. 14, and the hardness HV_5 ones, reported in Tables 3 and is constant (≈3).

4.2. Mechanisms leading to grain coarsening

Fatigue-assisted grain coarsening at low homologous temperature is a well-known phenomenon in nanocrystalline materials (grain size < 100 nm) where traditional intragranular dislocation mechanisms are suppressed and plasticity is governed by grain boundary sliding, grain boundary migration, and grain rotation (e.g., see Ref. [43]). In these materials, localized clusters of grains of larger size tend to form and here the collective activity of dislocations gives rise to persistent slip bands initiating the crack [44]. The phenomenon was also observed in some UFG metals (grain size in the range 100 nm-1μm) such as Al [45], Ti [46] and Cu [47–49] produced either by severe plastic deformation techniques or film electrodeposition, however the specific mechanisms are still an open problem and this work tries to shed more light on this aspect. Finally, to the best of our knowledge, only one case is reported in the literature [50] for metal alloys (Al 7075) with microcrystalline grains.

In the present experiments, the applied cyclic stress induces coarsening of grains and sub-grains, and a moderate increase of free dislocations inside the grains. The microstructural change is substantially homogeneous in the material without zones of stress accumulation (see KAM maps and distributions in Fig. 7).

Given the relevance of microstructural stability in nuclear applications, it is important to understand the mechanisms underlying the observed phenomena.

Since fatigue tests were carried out at low homologous temperature, well below $T/T_M = 0.5$, the motion of boundaries driven by volume or grain boundary self-diffusion is negligible. Also, grain rotation gives a very small contribution to the process leading to grain coarsening. In cyclic loading the grains tend to rotate toward the loading axis [50], and the angle Ω of lattice rotation can be calculated from the relationship:

$$\Omega = tan^{-1}(Nb < d >) \quad (6)$$

where $N = \pi(< d > /2)^2\rho$ is the average number of dislocations gliding through the slip planes. By introducing into Eq. (6) the data reported in Table 4 the angle of lattice rotation Ω is always <1° for all the fatigued samples. On these grounds, to identify the processes leading to grain coarsening, attention has been focused on (i) boundary migration and (ii) absorption in the boundaries of dislocations produced by Frank-Read (FR) sources inside the grains.

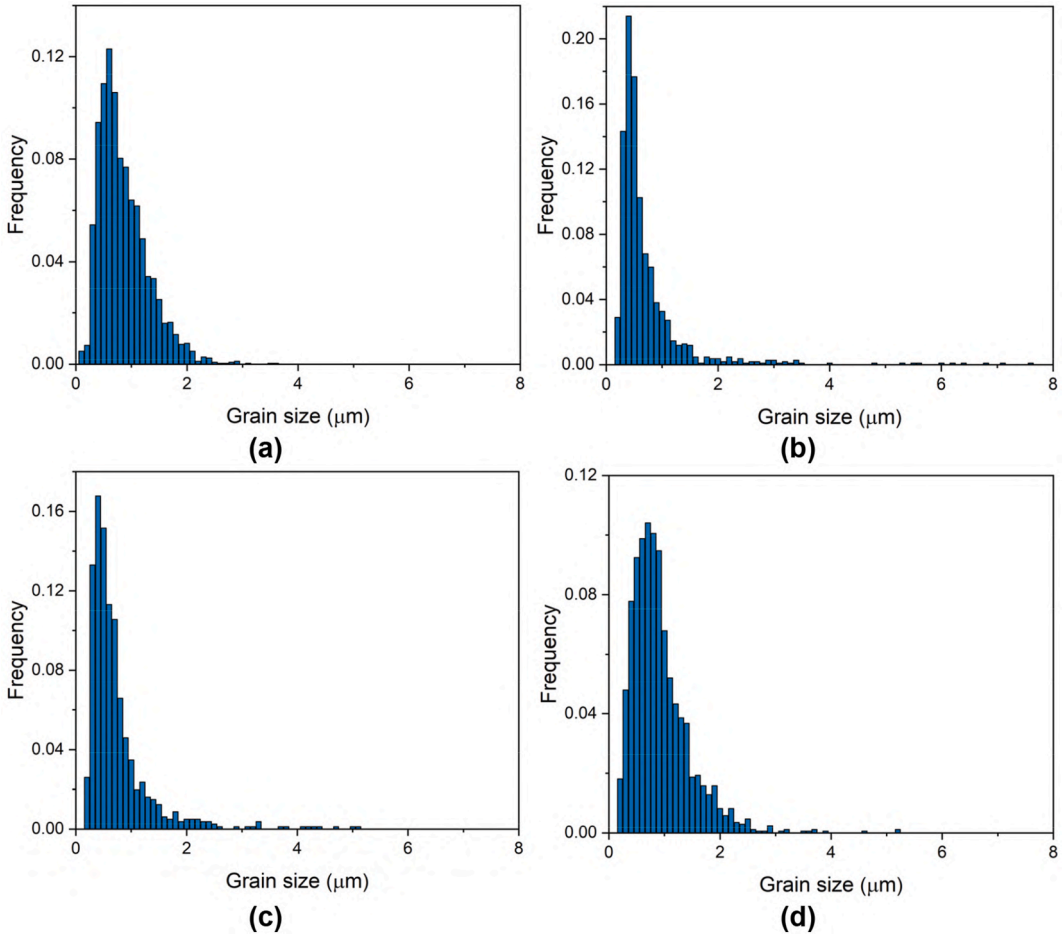

Fig. 5. Distributions of grain size determined from maps in Fig. 4 of samples 1 (a), 2 (b), 3 (c) and 4 (d).

(i) Boundary migration

TEM observations of original material and fatigued samples show that GBs have a regular shape. Waved GBs due to a local dislocation concentration near the boundary could originate an abnormal grain growth because of their greater mobility with respect to the planar ones. However, only a few irregularities were observed in our samples, which is consistent with homogeneous coarsening of grains and sub-grains.

Experimental results from various investigators have shown that a grain boundary can be driven by a mechanical stress field regardless of the angle of misorientation, i.e. whether it is HAGB or LAGB. According to the theoretical treatment of Gutkin and Ovid'ko [51] there is a critical shear stress τ_{C1} at which stable migration of the grain boundary starts to occur:

$$\tau_{C1} \approx \frac{G\Theta b}{2\pi(1-\upsilon)S} ln\frac{S}{b} \tag{7}$$

where $\upsilon = 0.3$ is the Poisson's ratio, Θ the misorientation between the grains, b the interatomic distance moved by each dislocation in the boundary (modulus of Burgers vector) and S the size of grains or sub-grains. The critical stress τ_{C1} increases with grain misorientation Θ, and Fig. 15 shows the trends for the fatigued samples 2, 3 and 4 calculated by introducing into Eq. (7) as S the $< D >$ values reported in Table 4. $< D >$ represents the smallest unit of crystal mosaic structure and, being the critical stress τ_{C1} approximately proportional to $1/S$, it corresponds to the most severe conditions for boundary migration.

Being the maximum shear stress τ the product of the Schmid factor ζ and the maximum applied stress, $= \zeta\, \sigma_{max}$, from the plots in Fig. 15 and the σ_{max} values in Table 2 it was possible to determine the maximum misorientation angle of boundaries which can migrate. This angle is 23, 32.5 and 40° for samples 2, 3 and 4, respectively. The result indicates that, under the present experimental conditions, all LAGBs are involved, whereas the involvement of HAGBs is partial and dependent on the applied stress. Based on the distributions of misorientation angles between the grains reported in Fig. 6, the calculated limit angles correspond to the following fractions of HAGBs which can migrate: 28 % (sample 2), 40 % (sample 3) and 51.5 % (sample 4).

Another critical stress τ_{C2} defines the limit of stable motion of a boundary [50]. This is expressed as:

$$\tau_{C2} = \frac{0.8G\Theta}{2\pi(1-\upsilon)} \tag{8}$$

If the external stress $\tau_{C1} < \tau < \tau_{C2}$ the motion is stable, while at $\tau > \tau_{C2}$ it becomes unstable, i.e. the grain boundary propagation does not depend on the level of τ. In the present experiments the condition expressed by Eq. (8) is valid if the misorientation angle $\Theta < 1°$, thus the occurrence of unstable motion involves few boundaries only and can be considered negligible.

(ii) Absorption in the boundaries of dislocations produced by FR sources inside the grains.

The other mechanism that can lead to instability and de-structuration of grain and sub-grain boundaries is the absorption into the boundaries of dislocations, generated by FR sources within the grains. The FR sources are usually dislocation segments pinned by carbides, however, the dislocation dipoles observed in fatigued samples (Fig. 11 (d)) can also act as FR sources. In Fe screw dislocations have low

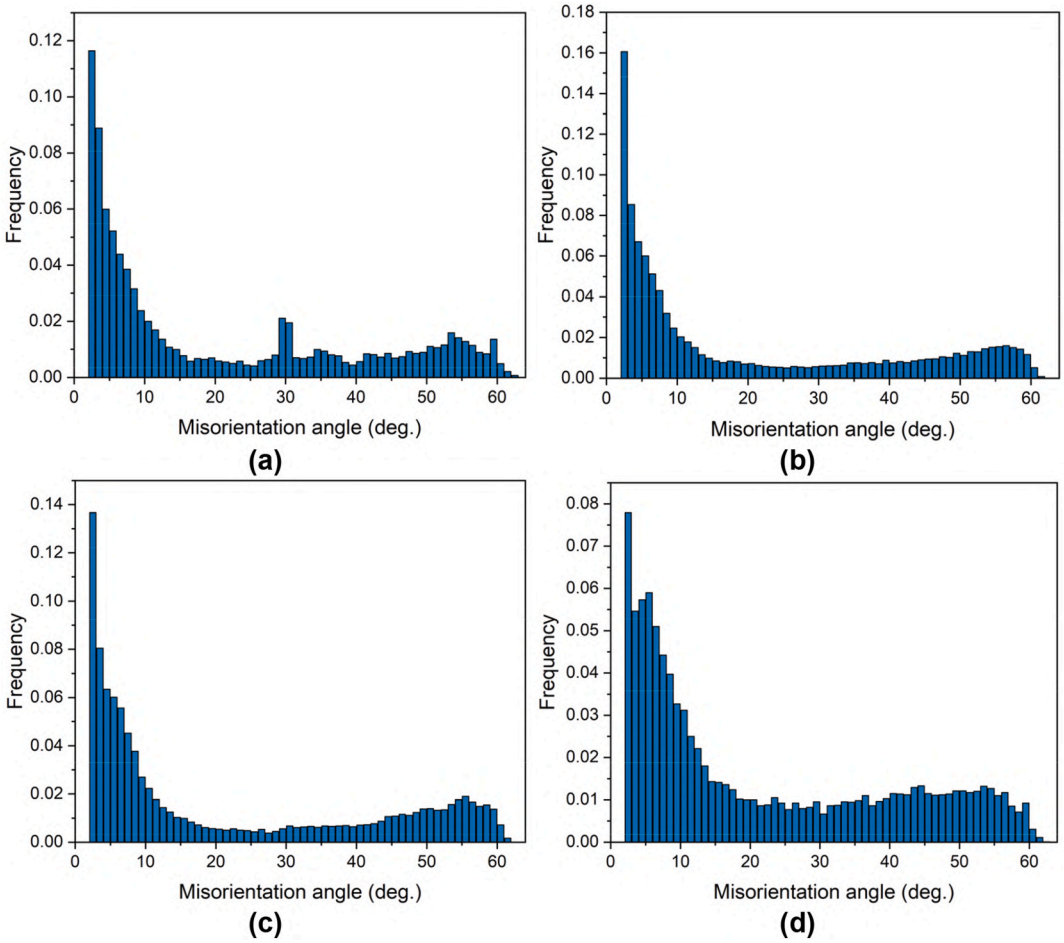

Fig. 6. Distributions of misorientation angles between the grains determined from maps in Fig. 4 of samples 1 (a), 2 (b), 3 (c) and 4 (d).

mobility whereas, under applied stress, the edge component in the dipole can move more easily, forming loops that act as FR sources.

If the external applied stress on a dislocation exceeds the critical barrier strength, the dislocation can penetrate the grain boundary. At this point, as outlined by Sutton and Balluffi [52], different cases may occur: direct transmission in the neighbor grain, transmission including residual dislocations in the GB, indirect transmission including residual dislocations in the GB where the incident and outgoing slip systems do not intersect, and no transmission with incorporation of the dislocation in the GB. This quite complex issue has been experimentally investigated for a long time and, more recently, also through modelling and discrete dislocation dynamics simulation [53].

The structure of an equilibrium GB consists of a network of Intrinsic Dislocations (IDs), which are geometrically necessary to accommodate the misorientation between the two crystals. After absorption of lattice dislocations through one of the aforesaid mechanisms, disordered networks of Extrinsic Dislocations (EDs) in the boundary can be formed. They represent an excess of dislocations and lead to a non-equilibrium boundary structure.

In most cases, the incident dislocation dissociates into an outgoing dislocation transmitted through the GB and a residual dislocation remaining within the GB, ultimately leading to an increasing number of dislocations at the grain boundary. The condition for dislocation transmission through a GB can be expressed as [53,54]:

$$\tau b_i^2 \geq \gamma_{gb} b_i + \alpha G (\Delta b)^2 \tag{9}$$

being τ the shear stress acting on the incoming dislocation, γ_{gb} the GB energy per unit area, $\alpha = 0.5$ a constant and $\Delta b = b_i - b_o$ the difference between the Burgers vectors of incoming (b_i) and outgoing (b_o) dislocations. For dislocation unit length, the term $\gamma_{gb} b_i$ is the energy needed to penetrate the GB while $\alpha G \Delta b^2$ represents the increase in GB energy due to the residual dislocation within the GB with Burgers vector Δb. The results of Yang et al. [54] indicate that as the GB misorientation angle increases, the critical stress τ required for dislocation penetration also increases. Thence, fewer dislocations penetrate the GB, thus promoting stress concentrations at the boundaries, which may trigger the formation of micro-cracks and micro-voids, like those observed on the fracture surfaces (Fig. 13).

By considering the stress involved in the present experiments and the energies calculated for different types of GBs in alpha Fe [55], the transmission of dislocations can take place only for a part of LAGBs.

Based on previous considerations, both GBs migration and absorption of lattice dislocations in the GBs contribute to induce GB instability, although the first mechanism seems to play a dominant role because it involves a greater fraction of boundaries.

Once GBs become unstable by incorporating an excess of dislocations, their disrupted structure may collapse. The complete collapse of GBs gives rise to the coarsening of grains and sub-grains and originates free or tangled dislocations. Annihilation may take place between dislocations of opposite signs below a critical distance, usually less than 50 nm, depending on crystal structure and microstructural features of the alloy. Anyway, as shown in Table 4, these events lead to an increase in dislocation density in the matrix, which remains modest, reaching one order of magnitude only in the sample tested under the highest applied stress (sample 4).

In the disordered structure of a non-equilibrium GB another process is likely to occur: part of EDs may move along the boundary itself with the result of GB sliding. The phenomenon is highlighted in the

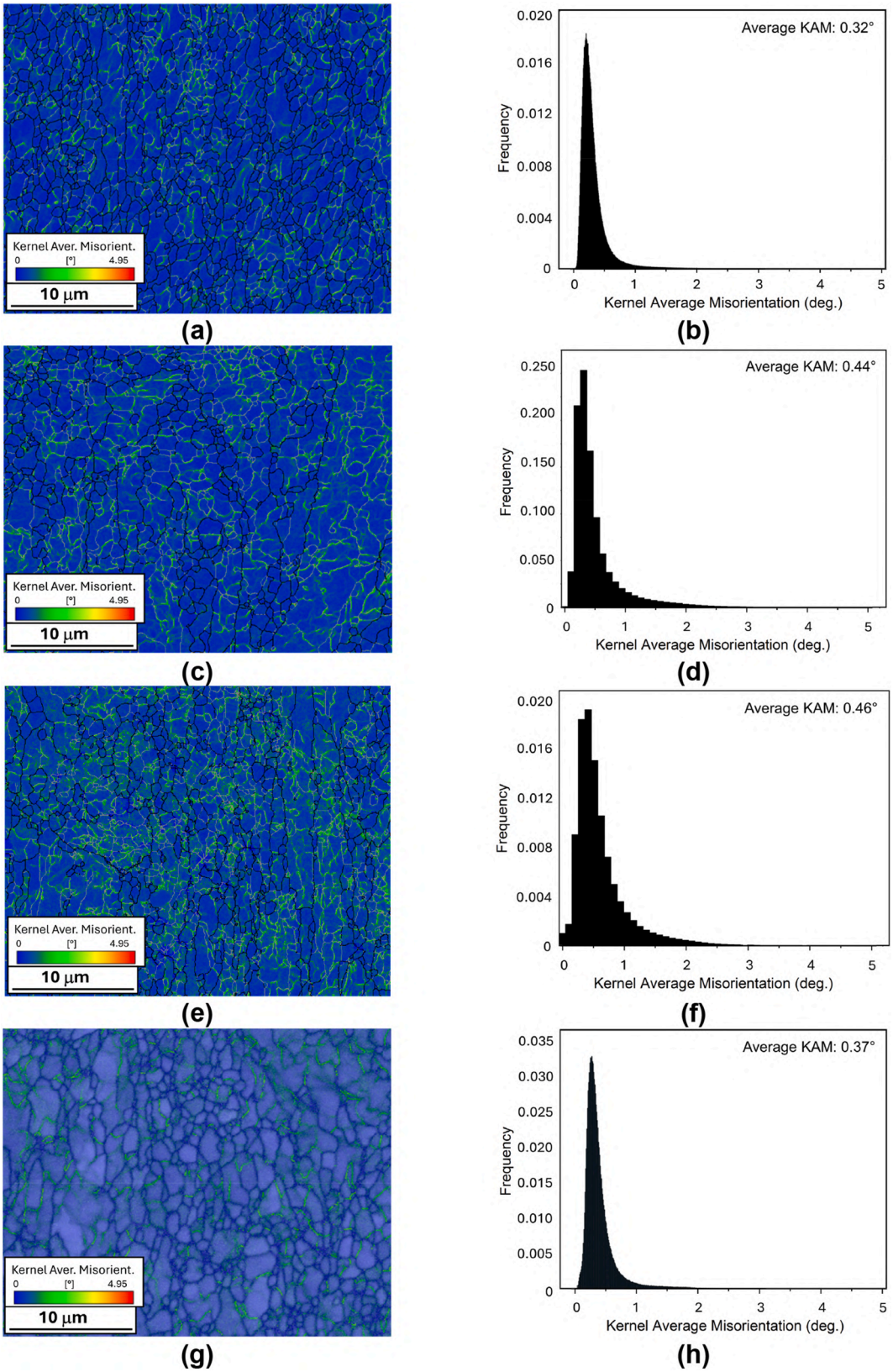

Fig. 7. KAM maps (a), (c), (e), (g) and distributions (b), (d), (f), (h) of samples 1 (a–b), 2 (c–d), 3 (e–f) and 4 (g–h).

micrograph of Fig. 13(c and d), showing slip bands emerging at the surface with thickness comparable to the average grain size. Of course, during GB sliding the grains with same orientation may merge and form a single grain of larger size.

Therefore, grain coarsening may take place either by GB collapse or GB sliding.

In conclusion, the process leading to grain coarsening proceeds through the following steps, which are schematically depicted in Fig. 16.

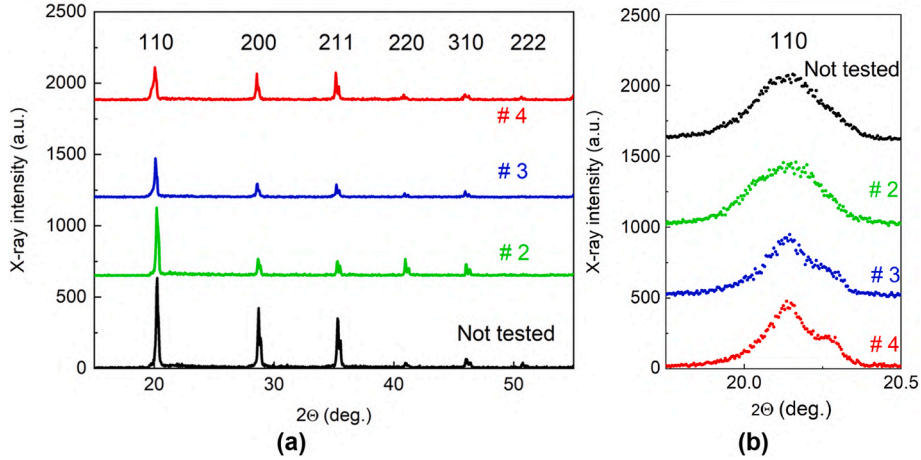

Fig. 8. XRD patterns (a) and {110} precision peak profiles (b) of the original material (not tested), compared to those of fatigued samples 2, 3 and 4.

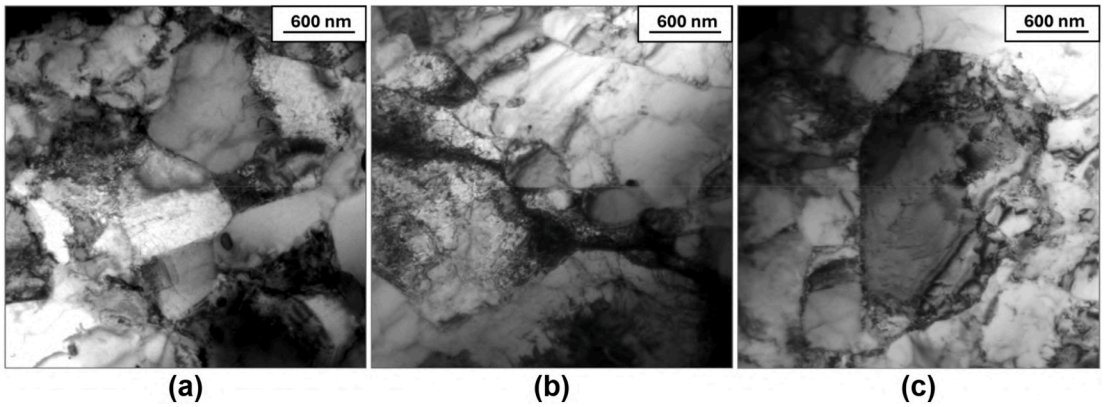

Fig. 9. Low-magnification BF-TEM micrographs showing the grain structure, and typical sub-grains, of samples 2 (a), 3 (b) and 4 (c).

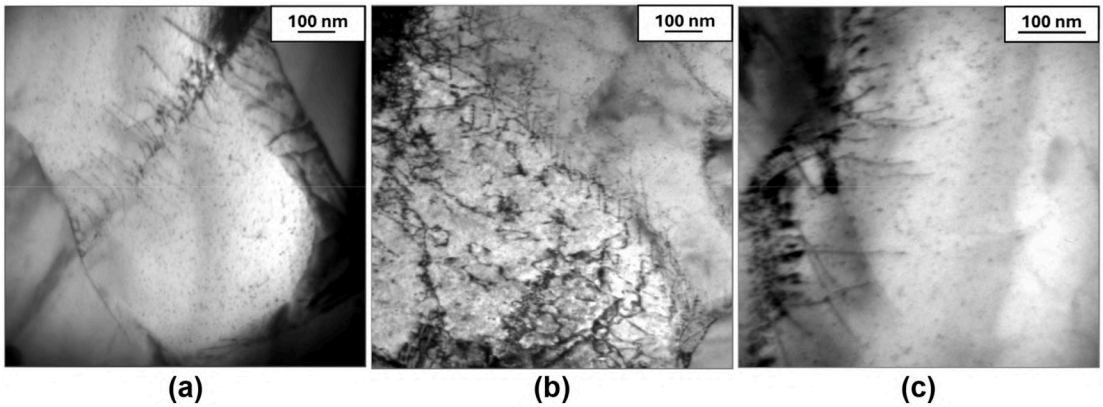

Fig. 10. BF-TEM showing the disaggregation of dislocations forming LAGBs and HAGBs in samples 2 (a), 3 (b) and 4 (c).

(i) the cyclic stress applied to the samples induces GB migration and activates FR dislocation sources inside the grains, which can be partly absorbed in GBs;
(ii) both mechanisms lead to an excess of dislocations in GBs;
(iii) part of such dislocations is re-emitted while another part is annihilated at the boundaries;
(iv) the remaining dislocations in excess give rise to an unstable condition;
(v) this could lead to either the collapse of GBs or sliding;
(vi) both these processes induce grain coarsening and consequent material softening.

4.3. *Relevance of fatigue softening to fusion applications*

Fatigue-induced softening was also observed in standard EUROFER97 [56–59] and other structural steels for nuclear fusion applications (P91 [60], P92 [61,62], MANET II and F82H [63]). The initial high strength of RAFMs, due to high dislocation density in a fine and well-dispersed precipitate distribution, can be seriously compromised

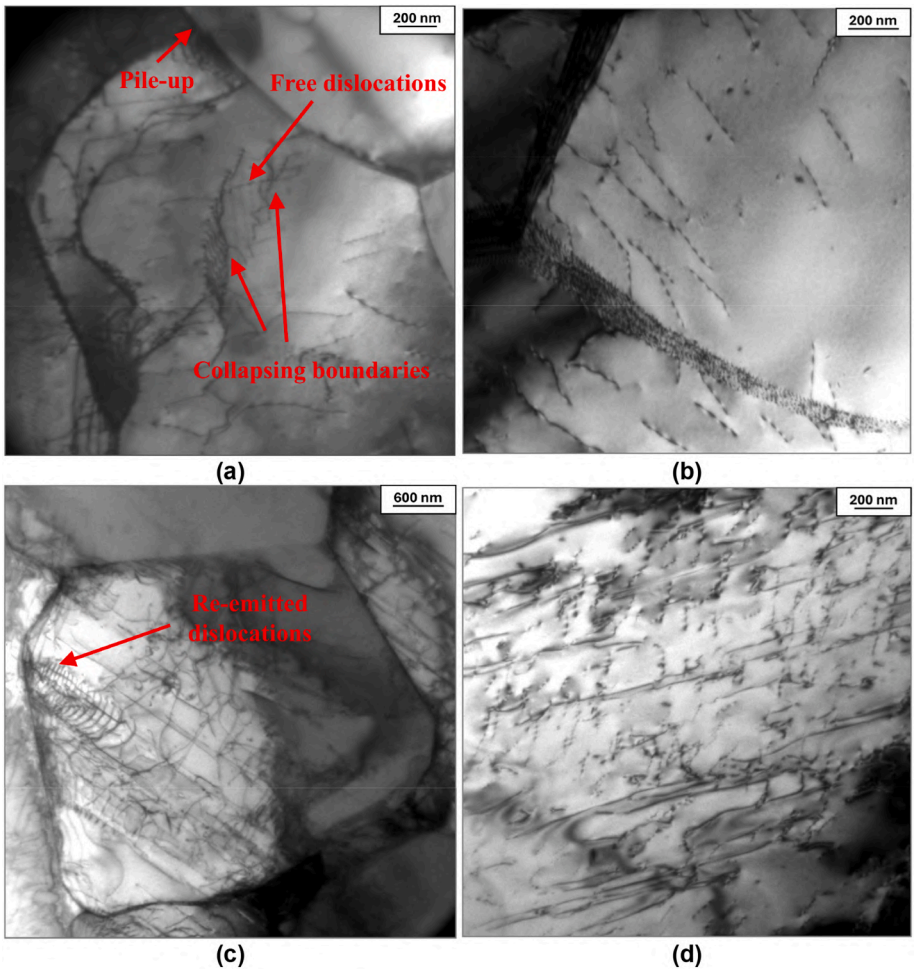

Fig. 11. Sample 4: the collapse of LAGBs give rise to free dislocations (a–b), dislocations re-emitted by a grain boundary indicated by red arrow (c) and dislocation dipoles (d).

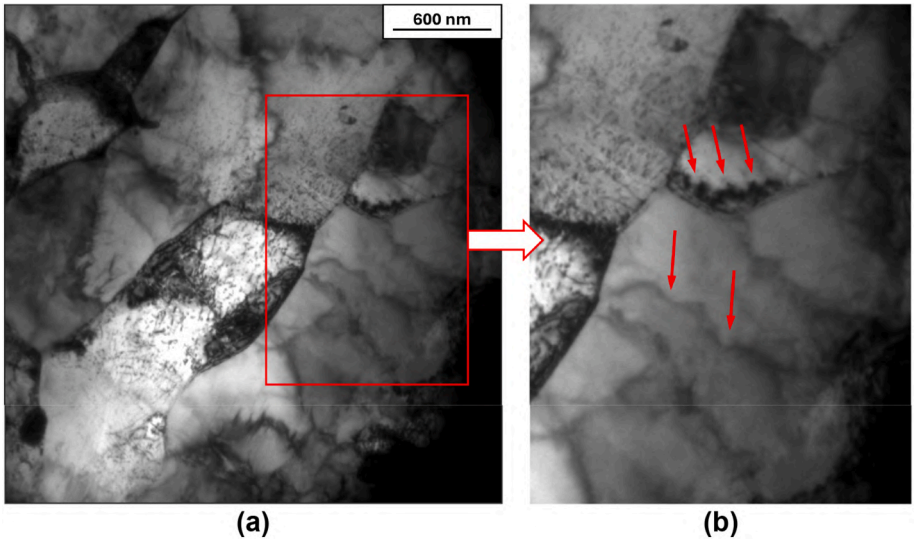

Fig. 12. Some waved boundaries are observed in sample 2 (a). This feature is displayed at higher magnification in (b).

under cyclic stress. In tests at room temperature softening of standard EUROFER97 is progressive with the number of cycles reaching a value of about 25 % before fracture (e.g. see Ref. [56]). The phenomenon, typical of ferritic-martensitic steels [64,65] both at room [66] and elevated temperature [67,68], is due to three main microstructural changes: (i) there is a reduction of free dislocations within the martensite laths because they accumulate at the grain and sub-grain boundaries; (ii) martensite laths split into sub-grains with a misorientation up to 5°; (iii)

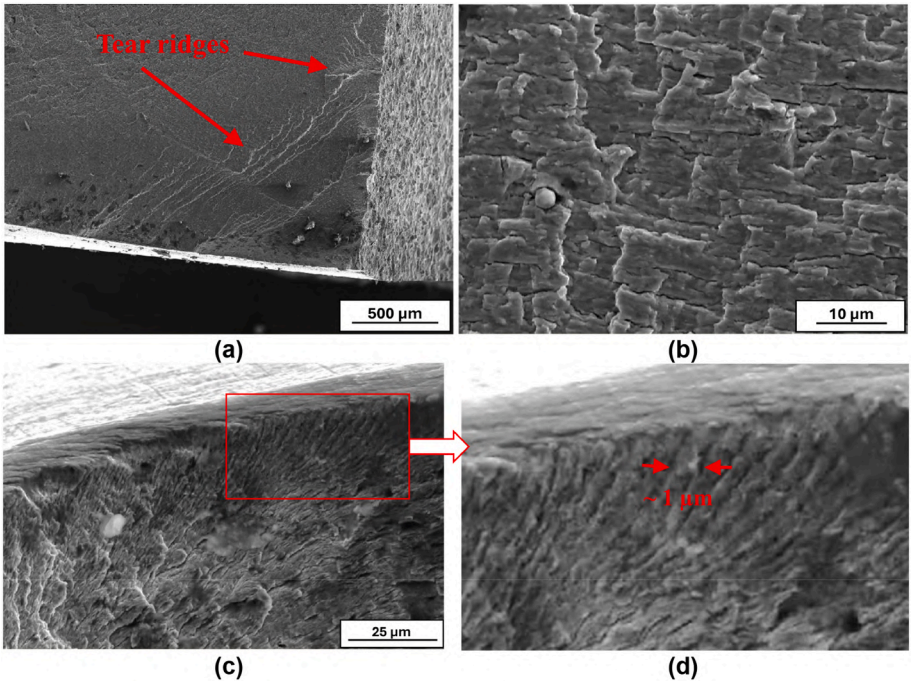

Fig. 13. SEM micrographs of the fracture surface of sample 4.

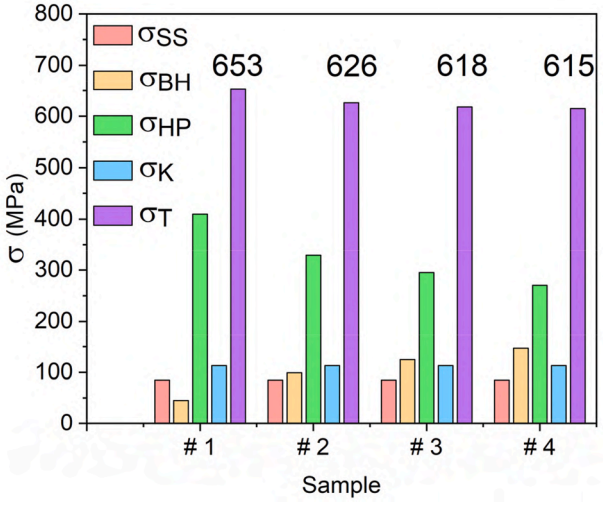

Fig. 14. Calculated strengthening contributions to yield stress of samples 1, 2, 3 and 4: solid solution (σ_{SS}), Bailey-Hirsch (σ_{BH}), Hall-Petch (σ_{HP}), Orowan (σ_K), and total strengthening (σ_T).

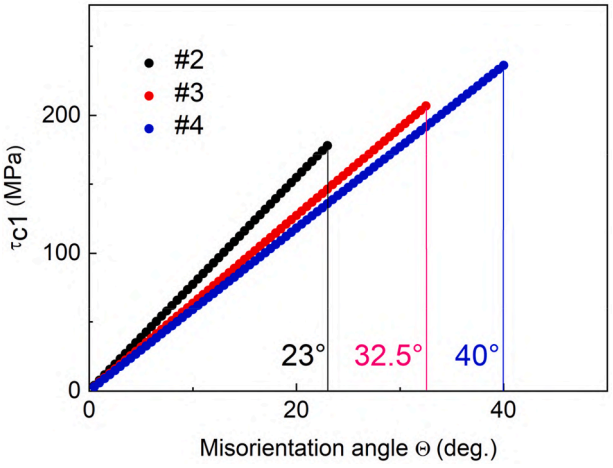

Fig. 15. Trends of τ_{C1} vs. the misorientation angle Θ for the fatigued samples 2, 3 and 4.

fatigue cells form from the largest grains, resulting in a homogeneous structure consisting of sub-grains of micrometric size. Softening due to sub-grains coalescence is enhanced by temperature increase up to 550 °C [56,69–71].

The microstructure obtained from the novel TMT guarantees better behavior in terms of softening: 5 % of UFG EUROFER97 vs. 25 % of standard EUROFER97. Moreover, the results of the present work identified GB migration as the primary mechanism responsible for boundary instability during cyclic deformation, ultimately leading to grain coarsening. Future work will therefore focus on modifying the microstructure to hinder this process and further reduce softening.

5. Conclusions

The present work investigated the mechanisms of fatigue softening in EUROFER97 steel prepared through the TMT developed by us, namely with a UFG microstructure, different from that of the standard material. The main results of the present work can be summarized as follows.

(i) HCF always induces grain and sub-grain coarsening with texture change, and dislocation density increase.
(ii) These microstructural changes have opposite effects on mechanical properties, however the resulting softening indicates that coarsening has the major impact.
(iii) The origin of grain and sub-grain coarsening is the instability of HAGBs and LAGBs when there is an excess of dislocations in the boundaries. Such a condition takes place following both boundary migration and absorption in the boundaries of dislocations produced by Frank-Read sources inside the grains, activated by cycling stress.
(iv) Unstable HAGBs and LAGBs lead to grain coarsening and texture variations through GB collapse or sliding. When an unstable

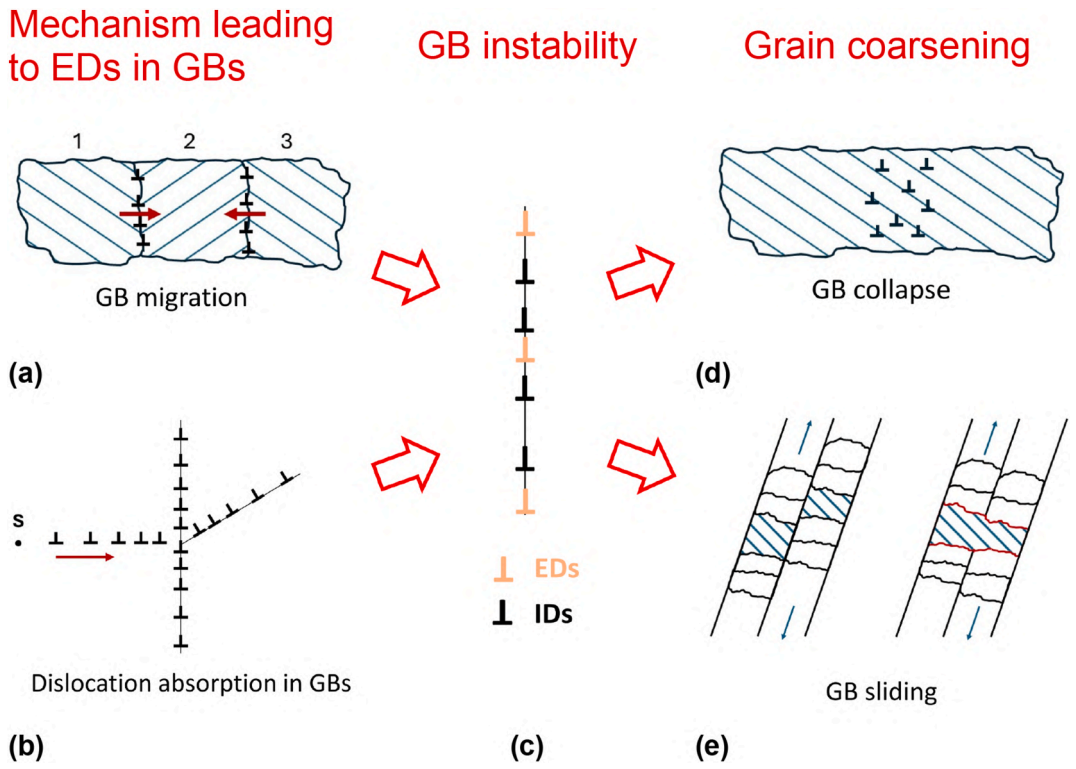

Fig. 16. Schematic representation of the process leading to grain coarsening. Two GBs migrate till to merge (a). The dislocations originated by the FR source S are in part transmitted in the neighbor grain and in part absorbed in the GB (b). Both mechanisms lead to an excess of dislocations (EDs) in GBs with consequent instability (c). Unstable GBs may either collapse releasing free dislocations (d) or slide (e) with consequent sub-grain and grain coarsening.

boundary collapses the dislocations that formed the boundary become free, thus a moderate increase in dislocation density accompanies grain coarsening.

(v) These microstructural changes lead to material softening: as applied stress increases, hardness decreases.

(vi) The novel TMT guarantees better behavior in terms of softening with respect to the standard EUROFER97 and the results will orientate future research to further reduce softening.

CRediT authorship contribution statement

Marcello Cabibbo: Investigation, Methodology, Writing-review and editing; Dario Croccolo: Investigation, Methodology, Writing-review and editing; Andrea Di Schino: Investigation, Writing-review and editing; Roberto Montanari: Conceptualization, Supervision, Writing-original draft; Giorgio Olmi: Investigation, Methodology, Data curation, Writing-review and editing; Giulia Stornelli: Investigation, Data curation, Writing-original draft; Claudio Testani: Investigation, Writing-review and editing. Alessandra Varone: Investigation, Methodology, Data curation, Writing-review and editing.

Funding

This research did not receive any specific grant from funding agencies in the public, commercial, or not-for-profit sectors.

Declaration of competing interest

The authors declare that they have no known competing financial interests or personal relationships that could have appeared to influence the work reported in this paper.

Data availability

Data will be made available on request.

References

[1] Balbaud-Célérier F, Cabet C. Materials and processes for nuclear energy today and in the future. Wiley; 2024. https://doi.org/10.1002/9781394325870.

[2] Gorley M, Diegele E, Gaganidze E, Gillemot F, Pintsuk G, Schoofs F, et al. The EUROfusion materials property handbook for DEMO in-vessel components—Status and the challenge to improve confidence level for engineering data. Fusion Eng Des 2020;158. https://doi.org/10.1016/j.fusengdes.2020.111668.

[3] Balbaud F, Cabet C, Cornet S, Dai Y, Gan J, Hernández Mayoral M, et al. A NEA review on innovative structural materials solutions, including advanced manufacturing processes for nuclear applications based on technology readiness assessment. Nuclear Materials and Energy 2021;27:101006. https://doi.org/10.1016/j.nme.2021.101006.

[4] Rieth M, Simondon E, Pintsuk G, Aiello G, Henry J, Terentyev D, et al. Technological aspects in blanket design: effects of micro-alloying and thermo-mechanical treatments of EUROFER97 type steels after neutron irradiation. Fusion Eng Des 2021;168:112645. https://doi.org/10.1016/j.fusengdes.2021.112645.

[5] Bhattacharya A, Chen X, Graening T, Geringer JW, Reed J, Henry J, et al. Irradiation hardening and ductility loss of Eurofer97 steel variants after neutron irradiation to ITER-TBM relevant conditions. Fusion Eng Des 2021;173:112935. https://doi.org/10.1016/j.fusengdes.2021.112935.

[6] Klimenkov M, Jäntsch U, Rieth M, Möslang A. Correlation of microstructural and mechanical properties of neutron irradiated EUROFER97 steel. J Nucl Mater 2020; 538:152231. https://doi.org/10.1016/j.jnucmat.2020.152231.

[7] Bohanon B, Wei P, Foster A, Bazar L, Zhang Y, Spearot D, et al. A critical review of irradiation-induced changes in reactor pressure vessel steels. Prog Nucl Energy 2024;174:105276. https://doi.org/10.1016/j.pnucene.2024.105276.

[8] Pilloni L, Cristalli C, Tassa O, Salvatori I, Storai S. Grain size reduction strategies on Eurofer. Nuclear Materials and Energy 2018;17:129–36. https://doi.org/10.1016/j.nme.2018.06.023.

[9] Kim BK, Tan L, Sakasegawa H, Parish CM, Zhong W, Tanigawa H, et al. Effects of helium on irradiation response of reduced-activation ferritic-martensitic steels: using nickel isotopes to simulate fusion neutron response. J Nucl Mater 2021;545: 152634. https://doi.org/10.1016/j.jnucmat.2020.152634.

[10] Zhou J, Shen Y, Jia N. Strengthening mechanisms of reduced activation ferritic/martensitic steels: a review. Int J Miner Metall Mater 2021;28:335–48. https://doi.org/10.1007/s12613-020-2121-1.

[11] Zinovev A, Chang C-C, Van Eyken J, Gaganidze E, Terentyev D. Effect of neutron irradiation to 0.7 dpa and 1.4 dpa on the tensile properties and fracture surface of EUROFER97 steel. J Nucl Mater 2023;587:154742. https://doi.org/10.1016/j.jnucmat.2023.154742.
[12] Gaganidze E, Gillemot F, Szenthe I, Gorley M, Rieth M, Diegele E. Development of EUROFER97 database and material property handbook. Fusion Eng Des 2018;135:9–14. https://doi.org/10.1016/j.fusengdes.2018.06.027.
[13] Chen X, Bhattacharya A, Sokolov MA, Clowers LN, Yamamoto Y, Graening T, et al. Mechanical properties and microstructure characterization of Eurofer97 steel variants in EUROfusion program. Fusion Eng Des 2019;146:2227–32. https://doi.org/10.1016/j.fusengdes.2019.03.158.
[14] Taylor N, Merrill B, Cadwallader L, Di Pace L, El-Guebaly L, Humrickhouse P, et al. Materials-related issues in the safety and licensing of nuclear fusion facilities. Nucl Fusion 2017;57:092003. https://doi.org/10.1088/1741-4326/57/9/092003.
[15] Puype A, Malerba L, De Wispelaere N, Petrov R, Sietsma J. Effect of processing on microstructural features and mechanical properties of a reduced activation ferritic/martensitic EUROFER steel grade. J Nucl Mater 2017;494:1–9. https://doi.org/10.1016/j.jnucmat.2017.07.001.
[16] Kachko O, Puype A, Terentyev D, Chang C-C, Rieth M, Petrov RH. Impact of neutron irradiation on the tensile properties of advanced EUROFER97-type steels. J Nucl Mater 2024;599:155176. https://doi.org/10.1016/j.jnucmat.2024.155176.
[17] Marzullo D, Spagnuolo GA, Aiello G, Boscary J, Graziosi G, Moscato I, et al. Selection of EU-DEMO divertor operating conditions: water cooling thermal-hydraulic parameters and power exhaust capabilities. Fusion Eng Des 2024;203:114467. https://doi.org/10.1016/j.fusengdes.2024.114467.
[18] Giancarli LM, Ahn M-Y, Cho S, Kawamura Y, Leal-Pereira A, Merola M, et al. Status of the ITER TBM Program and overview of its technical objectives. Fusion Eng Des 2024;203:114424. https://doi.org/10.1016/j.fusengdes.2024.114424.
[19] Pilloni L, Cristalli C, Tassa O, Bozzetto L, Zanin E, Bettocchi N. Development of innovative materials and thermal treatments for DEMO water cooled blanket. Nuclear Materials and Energy 2019;19:79–86. https://doi.org/10.1016/j.nme.2019.01.026.
[20] Cristalli C, Tassa O, Bozzetto L, Pilloni L. Achievement of Ultrafine Grain structure by means of recrystallization treatments. J Nucl Mater 2022;568:153852. https://doi.org/10.1016/j.jnucmat.2022.153852.
[21] Theodorou A, Schmid K, Schwarz-Selinger T. Annealing of hydrogen trap sites in displacement-damaged EUROFER. Nuclear Materials and Energy 2024;38:101595. https://doi.org/10.1016/j.nme.2024.101595.
[22] Mansur LF, Coghlan WA. Mechanisms of helium interaction with radiation effects in metals and alloys: a review. J Nucl Mater 1993;119–1:1–25. https://doi.org/10.1016/0022-3115(83)90047-8.
[23] Cristalli C, Pilloni L, Tassa O, Bozzetto L. Mechanical properties of several newly produced RAFM steels with Tungsten content in the range of 2 wt%. Nuclear Materials and Energy 2020;25:100793. https://doi.org/10.1016/j.nme.2020.100793.
[24] Karthikeyan T, Thomas Paul V, Saroja S, Moitra A, Sasikala G, Vijayalakshmi M. Grain refinement to improve impact toughness in 9Cr-1Mo steel through a double austenitization treatment. J Nucl Mater 2011;419:256–62. https://doi.org/10.1016/j.jnucmat.2011.08.010.
[25] Eddahbi M, Monge MA, Leguey T, Fernández P, Pareja R. Texture and mechanical properties of EUROFER 97 steel processed by ECAP. Mater Sci Eng 2011;528:5927–34. https://doi.org/10.1016/j.msea.2011.04.006.
[26] Song K, He G, Reza A, Ungár T, Karamched P, Yang D, et al. Microstructural and material property changes in severely deformed Eurofer-97. Mater Charact 2024;215:114144. https://doi.org/10.1016/j.matchar.2024.114144.
[27] Stornelli G, Montanari R, Testani C, Pilloni L, Napoli G, Di Pietro O, et al. Microstructure refinement effect on EUROFER 97 steel for nuclear fusion application. Mater Sci Forum 2021;1016 MSF:1392–7. https://dx.doi.org/10.4028/www.scientific.net/MSF.1016.1392.
[28] Stornelli G, Di Schino A, Mancini S, Montanari R, Testani C, Varone A. Grain refinement and improved mechanical properties of EUROFER97 by thermo-mechanical treatments. Applied Sciences (Switzerland) 2021;11:10598. https://doi.org/10.3390/app112210598.
[29] Stornelli G, Di Schino A, Montanari R, Testani C, Varone A. Assessment of mechanical properties and microstructure of EUROFER97 steel after thermo-mechanical treatments. Mater Sci Forum 2023;1105:47–52. https://doi.org/10.4028/p-t3IMA9.
[30] Stornelli G, Di Schino A, Montanari R, Sgambetterra M, Testani C, Varone A. Ultra-fine grained EUROFER97 steel for nuclear fusion applications. J Mater Res Technol 2024;33:5075–87. https://doi.org/10.1016/j.jmrt.2024.10.069.
[31] Lucon E, Vandermeulen W. Overview and Critical Assessment of the Tensile Properties of unirradiated and irradiated EUROFER97. Belgium; 2007.
[32] Zhang K, Walter M, Aktaa J. Ratcheting and fatigue behavior of Eurofer97 at high temperature, part 1: experiment. Fusion Eng Des 2020;150:111407. https://doi.org/10.1016/j.fusengdes.2019.111407.
[33] Zhao Y, Liang M, Liu S, Zhang W. High-temperature fatigue behavior and cyclic deformation of a gradient nanostructured RAFM steel. Int J Fatigue 2022;163:107013. https://doi.org/10.1016/j.ijfatigue.2022.107013.
[34] Croccolo D, Di Schino A, Montanari R, Olmi G, Stornelli G, Testani C, et al. High cycle fatigue response of grain refined EUROFER97. Int J Fatigue 2024;187:108442. https://doi.org/10.1016/j.ijfatigue.2024.108442.
[35] Correia JAFO, Zhu S, Berto F. Fatigue in advanced materials: advanced methods and applications. J Mater Res Technol 2023;26:4902–5. https://doi.org/10.1016/j.jmrt.2023.08.234.
[36] Lakshmanan A, Yaghoobi M, Stopka KS, Sundararaghavan V. Crystal plasticity finite element modeling of grain size and morphology effects on yield strength and extreme value fatigue response. J Mater Res Technol 2022;19:3337–54. https://doi.org/10.1016/j.jmrt.2022.06.075.
[37] ISO 1143. Metallic materials-rotating bar bending fatigue testing. 2010.
[38] JCPDS-International Centre for diffraction data. 1907. p. 2021. Newtown Square, PA, USA.
[39] Williamson GK, Smallman III RE. Dislocation densities in some annealed and cold-worked metals from measurements on the X-ray Debye-Scherrer spectrum. Philos Mag 1956;1:34–46. https://doi.org/10.1080/14786435608238074.
[40] Oliveira VB, Zilnyk KD, Sandim HRZ. Thermodynamic simulation of reduced activation ferritic–martensitic Eurofer-97 steel. J Phase Equilibria Diffus 2017;38:208–16. https://doi.org/10.1007/s11669-017-0530-2.
[41] Kocks UF, Mecking H. Physics and phenomenology of strain hardening: the FCC case. Prog Mater Sci 2003;48:171–273. https://doi.org/10.1016/S0079-6425(02)00003-8.
[42] Takaki S, Akama D, Nakada N, Tsuchiyama T. Effect of grain boundary segregation of interstitial elements on hall-petch coefficient in steels. Mater Trans 2014;55:28–34. https://doi.org/10.2320/matertrans.MA201314.
[43] Panzarino JF, Ramos JJ, Rupert TJ. Quantitative tracking of grain structure evolution in a nanocrystalline metal during cyclic loading. Model Simul Mat Sci Eng 2015;23:025005. https://doi.org/10.1088/0965-0393/23/2/025005.
[44] Boyce BL, Padilla HA. Anomalous fatigue behavior and fatigue-induced grain growth in nanocrystalline nickel alloys. Metall Mater Trans 2011;42:1793–804. https://doi.org/10.1007/s11661-011-0708-x.
[45] Mompiou F, Legros M, Boé A, Coulombier M, Raskin J-P, Pardoen T. Inter- and intragranular plasticity mechanisms in ultrafine-grained Al thin films: an in situ TEM study. Acta Mater 2013;61:205–16. https://doi.org/10.1016/j.actamat.2012.09.051.
[46] Zhao P, Chen B, Kelleher J, Yuan G, Guan B, Zhang X, et al. High-cycle-fatigue induced continuous grain growth in ultrafine-grained titanium. Acta Mater 2019;174:29–42. https://doi.org/10.1016/j.actamat.2019.05.038.
[47] Höppel HW, Zhou ZM, Mughrabi H, Valiev RZ. Microstructural study of the parameters governing coarsening and cyclic softening in fatigued ultrafine-grained copper. Philos Mag A 2002;82:1781–94. https://doi.org/10.1080/01418610208235689.
[48] Goto M, Kamil K, Han SZ, Euh K, Kim SS, Lee J. Fatigue-induced grain coarsening and crack growth behavior in ultrafine-grained copper under different loading histories. Int J Fatigue 2013;51:57–67. https://doi.org/10.1016/j.ijfatigue.2013.02.008.
[49] Goto M, Yakushiji T, Kim S, Yamamoto T, Han SZ. Formation process of fatigue slip bands with unique configurations of ultrafine-grained high-purity Cu fabricated by severe plastic deformation. J Alloys Compd 2022;899:163263. https://doi.org/10.1016/j.jallcom.2021.163263.
[50] Goswami R, Feng CR, Qadri SB, Pande CS. Fatigue-Assisted grain growth in Al alloys. Sci Rep 2017;7:10179. https://doi.org/10.1038/s41598-017-10889-8.
[51] Myu Gutkin, Ovid'ko IA. Grain boundary migration as rotational deformation mode in nanocrystalline materials. Appl Phys Lett 2005;87:251916. https://doi.org/10.1063/1.2147721.
[52] Sutton AP, Balluffi RW. Interfaces in crystalline materials. Oxford Science punlications; 1996.
[53] Li Z, Hou C, Huang M, Ouyang C. Strengthening mechanism in micro-polycrystals with penetrable grain boundaries by discrete dislocation dynamics simulation and Hall–Petch effect. Comput Mater Sci 2009;46:1124–34. https://doi.org/10.1016/j.commatsci.2009.05.021.
[54] Yang H, Zhang J, Jiang X. Study on dislocation-grain boundary penetration model and fracture behavior of poly-crystalline materials in the hydrogen environment. Acta Mech Solida Sin 2025;38:907–18. https://doi.org/10.1007/s10338-025-00605-9.
[55] Sarochawikasit R, Wang C, Kumam P, Beladi H, Okita T, Rohrer GS, et al. Grain boundary energy function for α iron. Materialia 2021;19:101186. https://doi.org/10.1016/j.mtla.2021.101186.
[56] Marmy P, Kruml T. Low cycle fatigue of Eurofer 97. J Nucl Mater 2008;377:52–8. https://doi.org/10.1016/j.jnucmat.2008.02.054.
[57] Gaisina E, Gaisin R, Leys J, Knitter R, Aktaa J, Walter M. Comparative analysis of low cycle fatigue behavior of pre-corroded standard and sub-sized EUROFER97 specimens exposed to ceramic breeder environment. Nuclear Materials and Energy 2023;36:101497. https://doi.org/10.1016/j.nme.2023.101497.
[58] Kuběna I, Polák J, Marmy P, Kruml T. A comparison of microstructure evolution due to fatigue loading in eurofer 97 and ODS eurofer steels. Procedia Eng 2014;74:401–4. https://doi.org/10.1016/j.proeng.2014.06.288.
[59] Giordana MF, Alvarez-Armas I, Armas A. Microstructural characterization of EUROFER 97 during low-cycle fatigue. J Nucl Mater 2012;424:247–51. https://doi.org/10.1016/j.jnucmat.2012.03.019.
[60] Kunz L, Lukáš P. High temperature fatigue and cyclic creep of P91 steel. In: European structural integrity Society, vol. 29. Elsevier; 2002. p. 37–44. https://doi.org/10.1016/S1566-1369(02)80060-7.
[61] Fournier B, Sauzay M, Pineau A. Micromechanical model of the high temperature cyclic behavior of 9–12%Cr martensitic steels. Int J Plast 2011;27:1803–16. https://doi.org/10.1016/j.ijplas.2011.05.007.
[62] Giroux PF, Dalle F, Sauzay M, Caës C, Fournier B, Morgeneyer T, et al. Influence of strain rate on P92 microstructural stability during fatigue tests at high temperature. Procedia Eng 2010;2:2141–50. https://doi.org/10.1016/j.proeng.2010.03.230.
[63] Armas AF, Petersen C, Schmitt R, Avalos M, Alvarez I. Cyclic instability of martensite laths in reduced activation ferritic/martensitic steels. J Nucl Mater 2004;329–333:252–6. https://doi.org/10.1016/j.jnucmat.2004.04.045.

[64] Sauzay M, Brillet H, Monnet I, Mottot M, Barcelo F, Fournier B, et al. Cyclically induced softening due to low-angle boundary annihilation in a martensitic steel. Mater Sci Eng 2005;400–401:241–4. https://doi.org/10.1016/j.msea.2005.02.092.

[65] Stubbins JF, Gelles DS. Fatigue performance and cyclic softening of F82H, a ferritic-martensitic steel. J Nucl Mater 1996;233–237:331–5. https://doi.org/10.1016/S0022-3115(96)00226-7.

[66] Verma P, Srinivas NCS, Singh SR, Singh V. Low cycle fatigue behavior of modified 9Cr–1Mo steel at room temperature. Mater Sci Eng 2016;652:30–41. https://doi.org/10.1016/j.msea.2015.11.060.

[67] Ahiale GK, Choi W-D, Cho S, Park Y-H, Chun Y-B, Oh Y-J. Low-Cycle fatigue behavior of reduced activation ferritic-martensitic steel at elevated temperatures. Met Mater Int 2023;29:71–80. https://doi.org/10.1007/s12540-022-01209-5.

[68] Wang Q, Wang Q, Gong X, Wang T, Zhang W, Li L, et al. A comparative study of low cycle fatigue behavior and microstructure of Cr-based steel at room and high temperatures. Mater Des 2020;195:109000. https://doi.org/10.1016/j.matdes.2020.109000.

[69] Dudova N, Mishnev R, Kaibyshev R. On the microstructural evolution in a 10% Cr martensitic steel during interrupted low cycle fatigue testing at 650 °C. Int J Fatigue 2023;175:107806. https://doi.org/10.1016/j.ijfatigue.2023.107806.

[70] Fukumoto K, Onitsuka T, Itoh T, Sakasegawa H, Tanigawa H. Microstructure of fatigue-tested F82H steel under multi-axial loadings. Nuclear Materials and Energy 2018;15:180–4. https://doi.org/10.1016/j.nme.2018.04.008.

[71] Zhao Y, Cao H, Liu S. The dislocation-based fatigue deformation mechanism of a RAFM steel under multi-axial loadings. J Nucl Mater 2022;558:153324. https://doi.org/10.1016/j.jnucmat.2021.153324.